


## Broadband Acoustic Ventilation Barriers

Man Sun,<sup>1</sup> Xinsheng Fang,<sup>1</sup> Dongxing Mao,<sup>1,\*</sup> Xu Wang,<sup>1,†</sup> and Yong Li<sup>1,2,‡</sup>

<sup>1</sup>*Institute of Acoustics, Tongji University, Shanghai 200092, China*

<sup>2</sup>*College of Architecture and Urban Planning, Tongji University, Shanghai 200092, China*

 (Received 16 January 2020; revised manuscript received 5 March 2020; accepted 23 March 2020; published 10 April 2020)

Conventional sound barriers impede airflow at the same time. Recent advances in acoustic metasurfaces provide a solution for air-permeable barriers utilizing the Fano-like interference. While the mechanism of Fano-like interference implies that such a realized device serves a narrow working frequency range around every destructive-interference frequency. Considering the fact that noise usually covers a wide frequency range, designing a broadband acoustic barrier is still a challenge. Here, we theoretically design a planar-profile and subwavelength-thickness (approximately  $\lambda/8$ ) acoustic ventilation barrier prohibitive for sound in a broad range. Our design is a metasurface consisting of a central hollow orifice and two surrounding helical pathways with varying pitch. Thanks to the hornlike helical pathways, the response strength from the monopolar and dipolar modes of the system almost keeps balance in the frequency range of interest, leading to an effective blocking of more than 90% of incident energy in the range of 900–1418 Hz. Experiments are conducted to validate the proposed design, whose results are consistent with the analytical predictions and simulations. The underlying working mechanism ensures the metasurface is capable of handling broadband sound coming from various directions. Our design has potential in air-permeable yet sound-proofing applications, such as simultaneously natural ventilation and noise reduction in green buildings.

DOI: [10.1103/PhysRevApplied.13.044028](https://doi.org/10.1103/PhysRevApplied.13.044028)

### I. INTRODUCTION

Conventional acoustic barriers designed for sound insulation block airflow transport at the same time. While in practice there are some particular scenarios calling for noise reduction and airflow passage simultaneously. For example, natural ventilation, a key component of green buildings, inevitably causes residents to suffer from the accompanying “invasive” noise. In pursuit of a sound-proofing yet airflow-permeating barrier, the common wisdom is to design a window allowing a winding airflow path with absorptive linings or perforated partitions [1–3]. In practice, a more winding lined path supports a more sufficient noise reduction, which in turn brings about a larger pressure drop, leading to a poorer ventilation effect. Hence, there has always been a trade-off between the efficiency of ventilation and noise reduction.

As a research area that has recently generated a proliferation of work, acoustic metasurfaces pave the way for sound manipulations with the advantages of their vanishing size and tremendous unique functionalities, such as anomalous refraction and reflection [4–15], hologram

rendering [16,17], and compact absorbers [18–22]. Recent advances in acoustic metasurface hold out possibilities for air-permeable barriers. Following this, acoustic ventilation barriers based on locally resonant units (Helmholtz resonators, membranes, quarter-wavelength tubes, etc.) are realized, which break the limitations of adjustable large-scale waves at subwavelength scales and enable a low-frequency noise reduction with a compact size [23–27]. Further efforts have also been taken to enhance the airflow passing, leading to binary-structured designs utilizing the Fano-like interference [28–30]. Such designs show the effectiveness of blocking low-frequency sound yet allowing a large airflow passage. However, let alone the former [23–27] based on local resonance only works at the resonant frequency, the mechanism of Fano-like interference implies that the latter [28–30] serves a narrow working frequency range around every destructive-interference frequency. Considering that noise usually covers a wide spectrum, designing a broadband acoustic ventilation barrier is still a challenge. Although efforts have been made to broaden the working frequency range by inducing multiple resonances, the resultant designs show either a limited bandwidth [31], or a largely degraded airflow passage [32].

In this work, we theoretically design and experimentally realize an acoustic ventilation barrier via a hollowed-out hornlike helical metasurface, which supports broadband

\*dxmao@tongji.edu.cn

†xuwang@tongji.edu.cn

‡yongli@tongji.edu.cn

sound reduction and large airflow passage simultaneously. Distinct from the general recipe, the broadband sound insulation is now realized by tuning the pitch variation of the helical pathway wheeling around the central orifice to achieve an almost balanced system's response strength between the monopolar and the dipolar modes in the frequency range of interest. Such a barrier effectively blocks more than 90% of incident sound energy in the range of 900–1418 Hz coming from various directions, while the structural thickness is only 5 cm (approximately  $\lambda/8$ ).

## II. META UNIT AND MODEL ANALYSIS

Figure 1(a) shows the general concept of our design, a binary structure with axisymmetric configuration. For a binary meta unit, the existing coupling between different parts implies that it is better to consider all the parts as the whole system. In what follows, we present a homogenization scheme for the ventilation barrier, which incorporates the eigenstate analysis that implies that the barrier's transmission and reflection behaviors can be depicted by its eigenstates. It indicates that the amplitudes of transmission and reflection can be determined with the analysis of strengths of the structure's all-independent response modes. According to the effective-medium theory, the central and surrounding parts are characterized by the refractive indices  $n_1$  and  $n_2$ , respectively. More generally, since the meta unit is in a subwavelength scale, the characteristics of the whole unit, with all structural complexities in its two parts, can be characterized by its Green function. The Green function can be expanded by the sum of all its eigenfunctions as [33]

$$G(z, z') = \sum_n \frac{p_n(z)p_n^*(z')}{(\omega_n^2 - \omega^2)/B_n}, \quad (1)$$

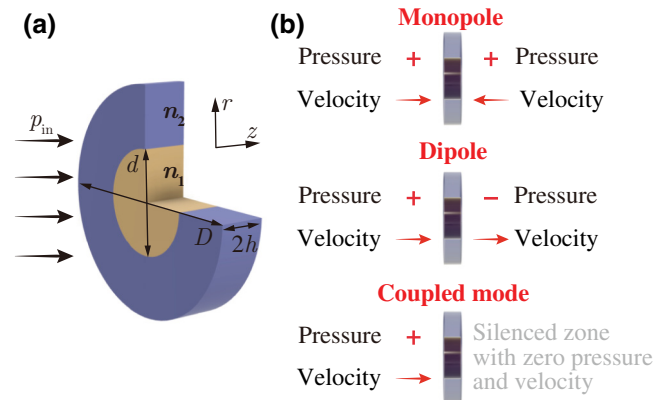


FIG. 1. (a) Schematic diagram of the binary meta unit placed perpendicular to the direction of wave propagation. The two-colored parts of the meta unit are characterized by two effective mediums with different acoustic properties. (b) Illustration of sound proofing induced from the equal-strength monopole and dipole responses of the meta unit.

where  $\omega_n$  is the  $n$ th eigen angular frequency,  $p_n(z)$  and  $p_n^*(z')$  are the eigenfunction and its conjugate of the  $n$ th eigenmode at the positions  $z$  and  $z'$ , respectively.  $B_n$  is the averaged modulus for the  $n$ th eigenmode, which can be calculated by the equation  $1/B_n = \int p_n(z)p_n^*(z)dV/(BS)$ , where the product of  $p_n$  and  $p_n^*$  is integrated over the whole volume of the meta unit,  $S$  is the cross-section area of the meta unit, and  $B$  is the local bulk modulus in air, i.e.,  $B = \rho_0 c_0^2$ . Here,  $\rho_0$  and  $c_0$  are density and velocity in air, respectively. In this one-dimensional (1D) scene, the meta unit's behaviors are completely described by the two modes: monopolar mode  $\bar{G}_+$  and dipolar mode  $\bar{G}_-$  [34], which can be expressed as

$$\bar{G}_+ = \omega^2 \sum_n \frac{p_n^*(h) [p_n(h) + p_n(-h)]}{(\omega_n^2 - \omega^2)/B_n}, \quad (2)$$

and

$$\bar{G}_- = \omega^2 \sum_n \frac{p_n^*(h) [p_n(h) - p_n(-h)]}{(\omega_n^2 - \omega^2)/B_n}. \quad (3)$$

Here  $h$  and  $-h$  are the coordinates of the front and back surfaces of the meta unit in  $z$  direction,  $p_n(h)$  and  $p_n(-h)$  are the corresponding averaged acoustic pressures related to the  $n$ th eigenmode, and  $p_n^*(h)$  is its conjugate. For a certain meta unit,  $\bar{G}_+$  and  $\bar{G}_-$  can be evaluated by Eqs. (2) and (3) with the use of the eigenfunctions and eigenfrequencies from eigenvalue calculations.

Based on the effective-medium theory, a meta unit can be equivalent to a homogenized medium of the same thickness, in which the effective wave number  $\bar{k}$  satisfies the equation

$$\left( \frac{\partial^2}{\partial z^2} + \bar{k}^2 \right) \bar{p}(z) = 0. \quad (4)$$

Once the monopolar and dipolar modes are obtained,  $\bar{k}$  can be straightforwardly determined, as [35]

$$\bar{k} = \frac{1}{h} \operatorname{arccot} \sqrt{-\frac{\bar{G}_+}{\bar{G}_-}}, \quad (5)$$

while the effective impedance  $\bar{Z}$  can be expressed as

$$\bar{Z} = -\frac{\bar{G}_+}{\omega \cot(\bar{k}h)}. \quad (6)$$

Finally, the transmission coefficient through the meta unit can be calculated by

$$T = \frac{4e^{2jh\bar{k}} \bar{Z} Z_0}{(\bar{Z} + Z_0)^2 - e^{4jh\bar{k}} (\bar{Z} - Z_0)^2}, \quad (7)$$

where  $Z_0$  is the acoustical characteristic impedance in air ( $Z_0 = \rho_0 c_0$ ) and  $j = \sqrt{-1}$ . Observing Eq. (5), one may

find an extreme case when  $\bar{G}_+ = \bar{G}_-$ , the effective wave number becomes pure imaginary infinity,  $\bar{k} \rightarrow j\infty$ , indicating the extreme attenuation of incident waves and a complete block of sound wave by the meta unit. This can be physically interpreted since now the system is with the same monopole and dipole response strength. As illustrated in Fig. 1(b), such a complete block is the result from the superposition of equal-strength monopole and dipole responses. In this particular condition, the effective impedance of the metasurface governed by Eq. (6) becomes an infinite-large reactance and the corresponding transmission coefficient described by Eq. (7) is theoretically zero. Both indicate now the metasurface behaves like an acoustic rigid boundary. As one can see in the following, even though the metasurface is a hollow-out design with a large air passage, such a condition renders a total reflection. Furthermore, the condition of  $\bar{G}_+ = \bar{G}_-$  implies a cross of the curves of monopole and dipole responses at the particular frequency. To further realize a broadband shielding, our strategy is to achieve multiple crosses, i.e., equal strength responded by monopolar and dipolar modes, in the frequency range of interest, as well as a consistently quasibalanced response strength among these crosses. In what follows, we show that, thanks to the presented methodology providing a comprehensive and accurate depiction on the barrier behavior, this can be readily achieved by engineering structural parameters of our proposed meta unit.

### III. HORNLIKE HELICAL META UNITS

To address the challenge of the broadband issue, here we design a binary meta unit, as shown by Fig. 2(a). It is a hornlike helical structure consisting of a central hollow orifice and two surrounding spiral blades creating hornlike helical pathways. These two parts are separated by a rigid cylindrical shell to eliminate the cross-coupling between them. Notice that, although the meta unit is similar to that proposed in Ref. [29], the distinct underlying mechanism (the Fano-like resonance for Ref. [29] and the consistently quasibalanced monopolar and dipolar response strength in a broadband for the present work) makes our design break the limitation of the narrow working frequency range. Here the central orifice serves as a passage to ensure sufficient air circulation, whose refractive index  $n_1 = 1$ . The outer hornlike helical part, which provides a varying refractive index  $n_2(z)$ , is designed for two reasons. The hornlike part provides a modest refractive index at the front and back surfaces of the meta unit to overcome the impedance mismatching in traditional designs [28,29] that usually relates to the narrow-band issue; while the hornlike pathways ensure that the whole meta unit possesses rich yet tunable surface responses of monopolar and dipolar modes to achieve high attenuation of sound energy within a frequency range of interest.

The geometries of the meta units are illustrated in Fig. 2(a), involving outer diameter  $D$ , inner diameter  $d$ , and thickness  $2h$ . Figure 2(b) shows the detailed internal construction of the helical part. Two varying-pitch helical layers are mirror-symmetrically arranged, which are then connected by the fix-pitch helical layer in between. The varying-pitch helices serve as impedance matching layers. The fix-pitch helix is induced, on one hand, to avoid the surrounding pathways over shrinking to hamper the sample fabrication in its finest part; while the length of the fix-pitch layer with respect to the whole helix ( $L/2h$ ) is an adjustable parameter in our design for tuning the surface responses. The spatial construct of the fix-pitch layers can be described by parametric equations, as [36]

$$\begin{cases} x = r \sin(\omega s), \\ y = r \cos(\omega s), & s \in [-s_0, s_0], \quad r \in [d/2, D/2], \\ z = as, \end{cases} \quad (8)$$

where  $r$  and  $\omega s$  represent the radius and angle of the blades, respectively;  $a$  is the parameter to describe the variable spacing of helical pitch. Inspired by the space-coiling metamaterials with varying cross-section channels [37–40], we propose a hornlike layer that can be described by

$$\begin{cases} x = r \sin(\omega s + \varphi), \\ y = r \cos(\omega s + \varphi), & s \in [s_1, s_2], \quad r \in [d/2, D/2], \\ z = e^s, \end{cases} \quad (9)$$

where  $\varphi$  is the initial phase used to ensure the continuity of blades at the interface between fix-pitch and hornlike layers. Compared to the fixed one, notice that now the development of the blades in the hornlike layers features an  $e$ -exponential growth in  $z$  direction. Since the pitch of thread  $P$  can be defined as the distance along with the unit's axis when each blade covers a complete rotation [36]. According to Eqs. (8) and (9), for the fix-pitch and hornlike layers, the corresponding thread pitches are  $P_{\text{fix}} = 2\pi a / \omega$  and  $P_{\text{horn}} = 2\pi e^s / \omega$ , indicating pathways of constant and hornlike cross section, respectively. The effective refractive index  $n_2(z)$  of the helical part can be defined as the ratio between the length of the wave-propagation path in the structure and its corresponding variance in the propagation direction ( $z$  direction), as

$$n_2(z) = \frac{dl}{dz} = \sqrt{\omega^2 r_e^2 \left(\frac{ds}{dz}\right)^2 + 1}, \quad (10)$$

where  $r_e$  is the effective radius of the helix, a fitted parameter equaling  $0.498D/2$  [36]. To overcome the impedance mismatching, at the front and back surfaces, the hornlike layers are expected to provide a modest  $n_2(\pm h)$ .

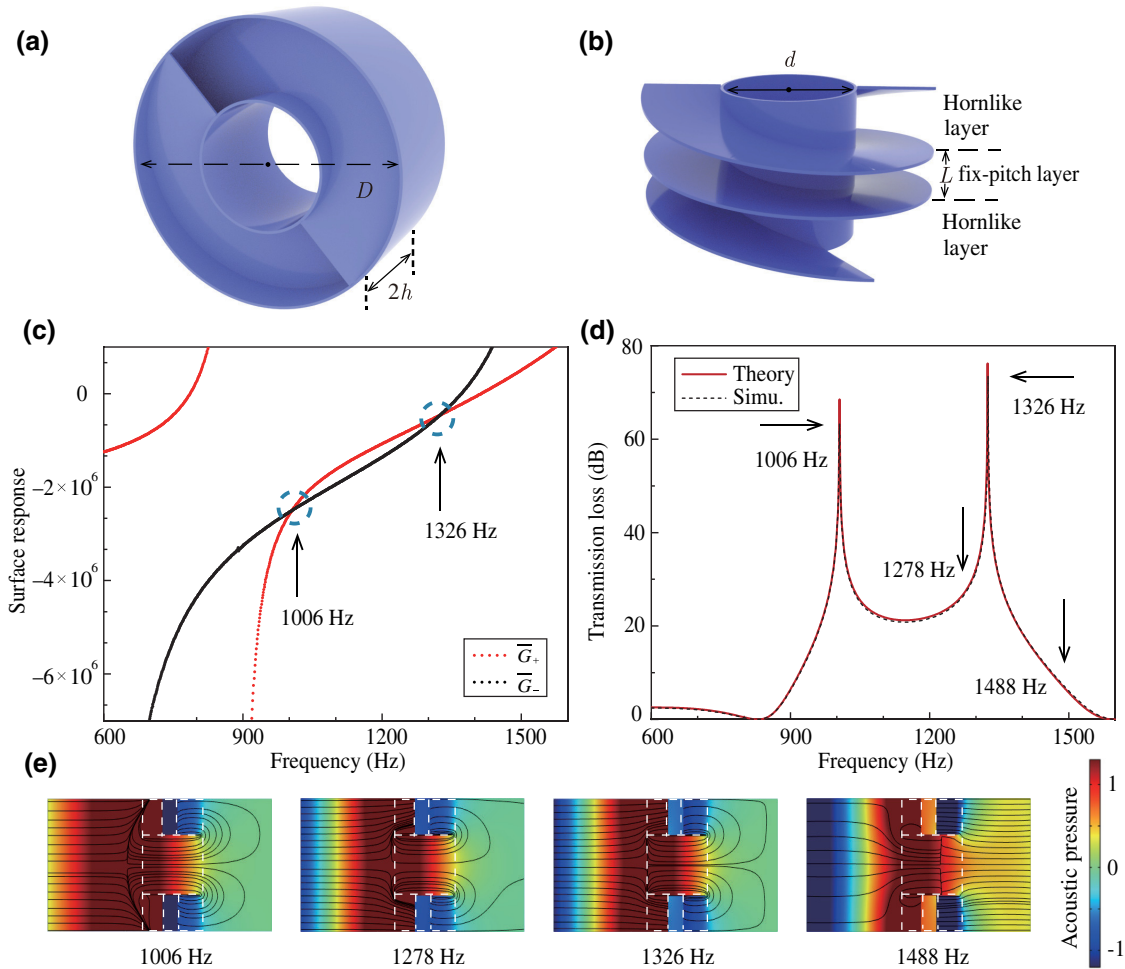


FIG. 2. (a) Realized meta unit with diameter  $D$  and thickness  $2h$ , which is composed of two parts: the central hollow-out orifice and a surrounding helix. (b) Internal structure of the helix. Two helical blades rotate around the central orifice creating two spiral pathways. The helix consists of three layers: two hornlike helical layers mirror-symmetrically arranged and connected by the fix-pitch helical layer of length  $L$  in between. The inner diameter of the hollow orifice is  $d$ , and the thicknesses of the cylindrical shell and blades are 1 mm. (c) Monopole and dipole response functions changing with frequency, depicted by red and black dots, respectively. These two curves intersect at 1006 and 1326 Hz. (d) Theoretically predicted (red curve) and numerically calculated (dashed black line) transmission loss of the helical meta unit. The frequency step is 1 Hz. Black arrows refer to four frequency points, the two peak frequencies, and a frequency between (beyond) the peak frequencies. (e) Simulated sound-field distributions at the four marked frequencies, where the black lines represent the local velocity streamlines, and the color maps illustrate the acoustic pressure distributions.

The rich geometrical parameters of the proposed hornlike meta unit provide great flexibility in tuning its acoustic property. For our design, by leveraging the three parameters: the relative diameter of central orifice ( $d/D$ ), the effective refractive index at the front and back surfaces [ $n_2(\pm h)$ ], as well as the relative length of fix-pitch layer ( $L/2h$ ), surface responses of the monopolar and dipolar

modes of the meta unit can be tailored to be almost balanced or even identical, without changing the structure outer profile. Table I lists the detailed geometries of a proof-of-concept meta unit specimen (diameter 100 and thickness 50 mm), which is designed with the optimized parameters  $d/D = 0.45$ ,  $n_2(\pm h) = 2.27$ , and  $L/2h = 0.35$ . According to the presented methodology, the barrier's

TABLE I. Geometrical parameters of the designed helical meta unit.

$D$ (mm)	$d$ (mm)	$h$ (mm)	$L$ (mm)	$\omega$ ( $\text{mm}^{-1}$ )	$a$	$s_0$ (mm)	$s_1$ (mm)	$s_2$ (mm)	$\varphi$
100.0	45.0	25.0	17.3	2.1	8.7	1.0	2.2	3.2	-2.4

performance, determined by the  $\bar{G}_+$  and  $\bar{G}_-$  profiles, is adjustable by tuning these parameters. This makes our design, in fact, provide a platform for realizing rich functionalities with target-set sound-shielding spectra.

#### IV. RESULTS AND DISCUSSIONS

Numerical simulations are carried out to verify the feasibility of our design by using the pressure acoustic module of COMSOL Multiphysics. First, the eigenfrequency study is performed, as required by Eqs. (8) and (9), to obtain the monopolar and dipolar modes ( $\bar{G}_+$  and  $\bar{G}_-$ ) of the designed meta unit. Figure 2(c) shows the calculated monopole and dipole response functions varying nonlinearly with frequency. Crosses between these curves are observed at 1006 and 1326 Hz, indicating the equal response strength by the monopolar and dipolar modes required by our broadband design. While in between the two intersections, it is observed that the response strengths of  $\bar{G}_+$  and  $\bar{G}_-$  remain close to each other over a fairly wide frequency range, which ensures a consistently low-transmission coefficient, i.e., high-transmission loss, in a broadband. Then, the frequency-domain study is performed to numerically calculate the sound transmission through the meta unit, where the designed meta unit is emplaced in a cylindrical waveguide, and both the waveguide and helical unit are considered acoustically rigid. Both ends of the waveguide are set as plane-wave radiation boundaries while the incident wave is only excited at one side. Figure 2(d) shows the transmission loss of the designed meta unit from both theoretical calculations using Eq. (7) and numerical simulations, showing an excellent agreement. Moreover, both

results confirm the complete sound blocking at 1006 and 1326 Hz. To gain a deeper insight into the performance of the designed meta unit, Fig. 2(e) shows the numerical results of the distributions of sound-pressure and particle-velocity streamlines on a cut plane. At peak frequencies of 1006 and 1326 Hz, the color maps show a dramatic reduction of pressure amplitude through the meta unit, providing a completely silenced zone behind; while the streamlines featuring a curvature pattern behind the unit demonstrate a strong coupling between the helical part and the central part, resulting in a diminished radiation in the far field. Between the two peaks, the simulated result shows a very similar pattern, i.e., a remarkably degraded amplitude and localized streamlines, indicating that sound blocking is not only confined at these two peak frequencies, but is consistently effective in the whole frequency range in between. Beyond this range [the rightmost one in Fig. 2(e)], the sound field shows a totally different pattern: although pressure amplitude is decreased, the streamlines parallel to the waveguide axis confirm a propagating transmitted wave, accompanied with a large amount of “leaked” sound energy.

The experiment is carried out to verify the designed meta unit. Figure 3(a) shows the sample of the meta unit made of photosensitive resin via 3D printing, with the thicknesses of the cylindrical shell and helical blades of 1 mm. The transfer matrix method is adopted to measure the transmission loss of the meta unit by using a Brüel and Kjær type-4206 impedance tube, as illustrated in Fig. 3(b). In the experiment, the sample is fixed firmly with clamps in the impedance tube. As shown in Fig. 3(c), a good agreement among theoretical calculation, simulation, and

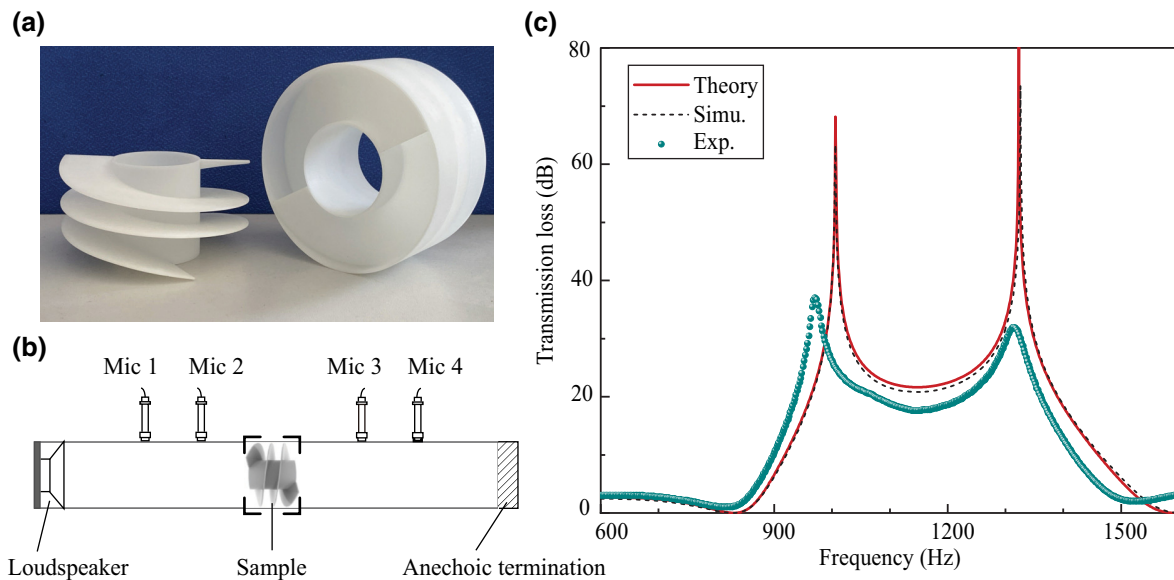


FIG. 3. (a) Photo of the 3D-printed specimen of the designed helical meta unit. (b) Schematics of the experimental setup where the specimen is clamped in the Brüel and Kjær type-4206 impedance tube. (c) Theoretical (red line), simulated (black dashed line), and measured (green dots) transmission loss of the designed helical meta unit.

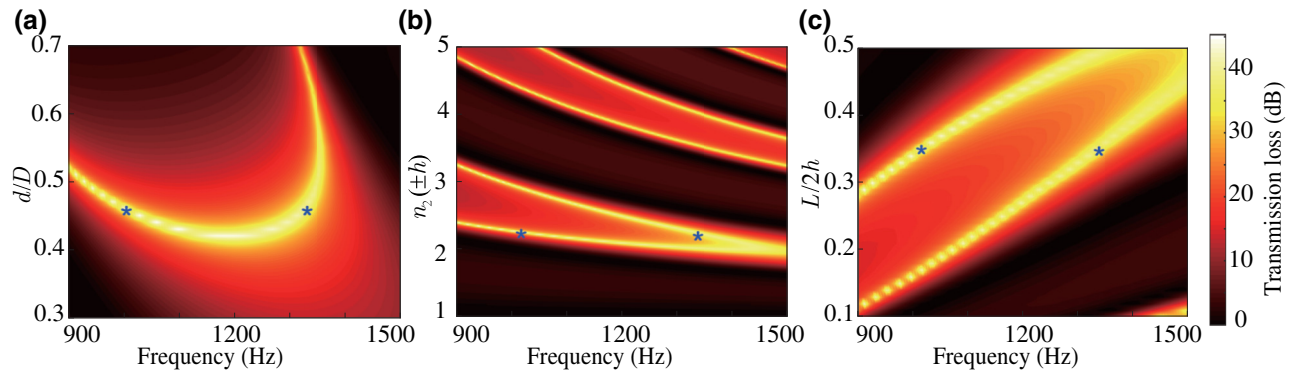


FIG. 4. Transmission loss varying with (a) the relative diameter of central orifice  $d/D$ , (b) the effective refractive index at the front and back surfaces  $n_2(\pm h)$ , and (c) the relative length of fix-pitch layer  $L/2h$ . In these colormaps, the bright regions represent effectively silenced zones. Stars in the colormap show those points correspond to the selected system parameters and the frequency with a peak transmission (1006 and 1326 Hz) in our design.

experiment demonstrates the effectiveness of the designed meta unit. Such an acoustic barrier blocks more than 90% of incident sound energy in the range of 900–1418 Hz (experimental data). Compared to its precedent [29], such a broadband feature expands the scope of the practicability of our design.

As aforementioned, the proposed hornlike meta unit provides great flexibility on tailoring its acoustic property, leading to an adjustable frequency band by tuning the system parameters, without changing the structure outer profile ( $D = 100$  mm,  $2h = 50$  mm). Figure 4(a) shows the transmission loss as a function of blue stars in the colormap indicate two extreme points referring to the zero transmission, the complete sound blocking resulted from equal-strength responses of monopolar and dipolar eigenmodes. Since there are two special frequency points satisfying this relationship, the silenced zone (the bright regions) is significantly extended. It shows that this phenomenon only exists in a small range, i.e.,  $d/D \in (0.44, 0.52)$ , in which  $d/D = 0.45$  creates the widest silenced band. Figure 4(b) shows the colormap with varying  $n_2(\pm h)$ . In fact, a similar phenomenon also occurs at higher  $n_2(\pm h)$ . While a larger  $n_2(\pm h)$  indicates a stronger impedance mismatching, and hence leads to a narrower bandwidth. In this case,  $n_2(\pm h) = 2.27$  is an optimal value. Figure 4(c) illustrates the case with varying length of fix-pitch layer  $L/2h$ . Although the silenced range extends with  $L/2h$ , the two yellow curves show a complete blocking blur at the same time, indicating that there is no total reflection for a larger  $L/2h$ .

In practice, the functionality of an acoustic barrier should not restrict to only normal incidence. In fact, the nature of a metasurface made up of subwavelength units suggests that the meta unit itself provides a motion-constraint condition to the particles, leading to a one-dimensional sound field along the central or helical path, regardless of the incident angle. We numerically inspect

the transmittance through the proposed acoustic barrier under oblique incidence (Fig. 5). The simulation results show that the broadband characteristic is observable under a wide-angle range of incidence. The complete blocking under oblique incidence occurs at precisely the same frequencies as that under normal incidence, while the sound blocking even becomes better at other frequencies under oblique incidence.

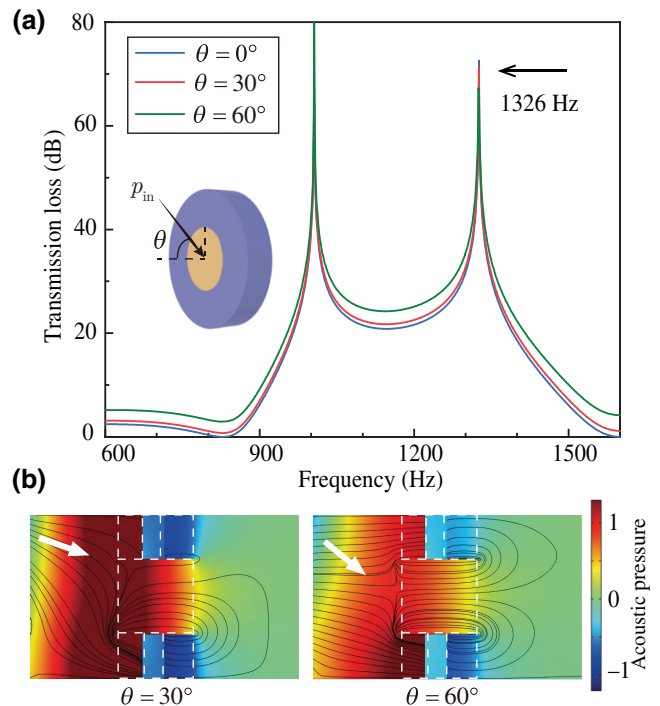


FIG. 5. (a) Transmission loss of pressure when plane waves come with incident angles of  $0^\circ$  (blue line),  $30^\circ$  (red line), and  $60^\circ$  (green line), respectively. (b) The simulated sound-field distributions with incidence angles of  $30^\circ$  and  $60^\circ$  at a peak frequency of 1326 Hz.

## V. CONCLUSIONS

To conclude, we theoretically design a planar-profile and subwavelength-thickness acoustic barrier, which is transparent to airflow while prohibitive for sound in a broad range. We show that the proposed hornlike meta unit provides great flexibility on tailoring its acoustic property, leading to the hybrid states contributed by equal-strength responses of monopolar and dipolar eigenmodes in the frequency range of interest. Experiments are conducted to validate the proposed design, such a design effectively blocks 90% of incident energy in the range of 900–1418 Hz, while its structural thickness is only 50 mm (approximately  $\lambda/8$ ). The rich geometrical parameters offer our design an adjustable frequency behavior, while the subwavelength nature ensures that it is capable of handling sound waves coming from different angles. Our design offers a solution for shielding acoustic wave in such a compact and opened manner without impeding airflow, and more essentially, suggests an efficient approach towards on-demand flow-permeable acoustic impedance engineering in broadband.

## ACKNOWLEDGMENTS

This work is financially supported in part by the National Science Foundation of China under Grants No. 11774265, No. 11704255, and No. 11704284) and the Young Elite Scientists Sponsorship by CAST (Grant No. 2018QNRC001).

- 
- [1] J. Kang and M. W. Brocklesby, Feasibility of applying micro-perforated absorbers in acoustic window systems, *Appl. Acoust.* **66**, 669 (2005).
- [2] X. Yu, S. K. Lau, L. Cheng, and F. Cui, A numerical investigation on the sound insulation of ventilation windows, *Appl. Acoust.* **117**, 113 (2017).
- [3] N. Yuya, N. Sohei, N. Tsuyoshi, and Y. Takashi, Sound propagation in soundproofing casement windows, *Appl. Acoust.* **70**, 1160 (2009).
- [4] Y. Li, B. Liang, Z. M. Gu, X. Y. Zou, and J. C. Cheng, Reflected wavefront manipulation based on ultrathin planar acoustic metasurfaces, *Sci. Rep.* **3**, 2546 (2013).
- [5] J. Zhao, B. Li, Z. Chen, and C. W. Qiu, Manipulating acoustic wavefront by inhomogeneous impedance and steerable extraordinary reflection, *Sci. Rep.* **3**, 2537 (2013).
- [6] Y. Li, X. Jiang, R. Q. Li, B. Liang, X. Y. Zou, L. L. Yin, and J. C. Cheng, Experimental Realization of Full Control of Reflected Waves with Subwavelength Acoustic Metasurfaces, *Phys. Rev. Appl.* **2**, 064002 (2014).
- [7] K. Tang, C. Qiu, M. Ke, J. Lu, Y. Ye, and Z. Liu, Anomalous refraction of airborne sound through ultrathin metasurfaces, *Sci. Rep.* **4**, 6517 (2014).
- [8] J. Mei and Y. Wu, Controllable transmission and total reflection through an impedance-matched acoustic metasurface, *New J. Phys.* **16**, 123007 (2014).
- [9] Y. Xie, W. Wang, H. Chen, A. Konneker, B.-I. Popa, and S. A. Cummer, Wavefront modulation and subwavelength diffractive acoustics with an acoustic metasurface, *Nat. Commun.* **5**, 5553 (2014).
- [10] Y. Li, X. Jiang, B. Liang, J. C. Cheng, and L. K. Zhang, Metascreen-Based Acoustic Passive Phased Array, *Phys. Rev. Appl.* **4**, 024003 (2015).
- [11] C. Shen, Y. Xie, J. Li, S. A. Cummer, and Y. Jing, Asymmetric acoustic transmission through near-zero-index and gradient-index metasurfaces, *Appl. Phys. Lett.* **108**, 223502 (2016).
- [12] Y. Li, C. Shen, Y. Xie, J. Li, W. Wang, S. A. Cummer, and Y. Jing, Tunable Asymmetric Transmission via Lossy Acoustic Metasurfaces, *Phys. Rev. Lett.* **119**, 035501 (2017).
- [13] B. Assouar, B. Liang, Y. Wu, Y. Li, J. C. Cheng, and Y. Jing, Acoustic metasurfaces, *Nat. Rev. Mater.* **3**, 460 (2018).
- [14] X. Wang, X. Fang, D. Mao, Y. Jing, and Y. Li, Extremely Asymmetrical Acoustic Metasurface Mirror at the Exceptional Point, *Phys. Rev. Lett.* **123**, 214302 (2019).
- [15] S.-W. Fan, S.-D. Zhao, A. L. Chen, Y.-F. Wang, B. Assouar, and Y.-S. Wang, Tunable Broadband Reflective Acoustic Metasurface, *Phys. Rev. Appl.* **11**, 044038 (2019).
- [16] Y. Xie, C. Shen, W. Wang, J. Li, D. Suo, B.-I. Popa, Y. Jing, and S. A. Cummer, Acoustic holographic rendering with two-dimensional metamaterial-based passive phased array, *Sci. Rep.* **6**, 35437 (2016).
- [17] Y. Zhu, J. Hu, X. Fan, J. Yang, B. Liang, X. Zhu, and J. Cheng, Fine manipulation of sound via lossy metamaterials with independent and arbitrary reflection amplitude and phase, *Nat. Commun.* **9**, 1632 (2018).
- [18] G. Ma, M. Yang, S. Xiao, Z. Yang, and P. Sheng, Acoustic metasurface with hybrid resonances, *Nat. Mater.* **13**, 873 (2014).
- [19] Y. Li and B. M. Assouar, Acoustic metasurface-based perfect absorber with deep subwavelength thickness, *Appl. Phys. Lett.* **108**, 063502 (2016).
- [20] S. Huang, X. Fang, X. Wang, B. Assouar, Q. Cheng, and Y. Li, Acoustic perfect absorbers via spiral metasurfaces with embedded apertures, *Appl. Phys. Lett.* **113**, 233501 (2018).
- [21] S. Huang, X. Fang, X. Wang, B. Assouar, Q. Cheng, and Y. Li, Acoustic perfect absorbers via helmholtz resonators with embedded apertures, *J. Acoust. Soc. Am.* **145**, 254 (2019).
- [22] S. Huang, Z. Zhou, D. Li, T. Liu, X. Wang, J. Zhu, and Y. Li, Compact broadband acoustic sink with coherently coupled weak resonances, *Sci. Bull.* **65**, 373 (2020).
- [23] G. Ma, M. Yang, Z. Yang, and P. Sheng, Low-frequency narrow-band acoustic filter with large orifice, *Appl. Phys. Lett.* **103**, 011903 (2013).
- [24] S.-H. Kim and S.-H. Lee, Air transparent soundproof window, *AIP Adv.* **4**, 117123 (2014).
- [25] N. Jiménez, V. Romero-García, V. Pagneux, and J.-P. Groby, Rainbow-trapping absorbers: Broadband, perfect and asymmetric sound absorption by subwavelength panels for transmission problems, *Sci. Rep.* **7**, 13595 (2017).
- [26] C. Shen, Y. Xie, J. Li, S. A. Cummer, and Y. Jing, Acoustic metacages for sound shielding with steady air flow, *J. Appl. Phys.* **123**, 124501 (2018).
- [27] X. Wu, K. Y. Au-Yeung, X. Li, R. C. Roberts, J. Tian, C. Hu, Y. Huang, S. Wang, Z. Yang, and W. Wen,

- High-efficiency ventilated metamaterial absorber at low frequency, *Appl. Phys. Lett.* **112**, 103505 (2018).
- [28] H. L. Zhang, Y. F. Zhu, B. Liang, J. Yang, J. Yang, and J. C. Cheng, Omnidirectional ventilated acoustic barrier, *Appl. Phys. Lett.* **111**, 203502 (2017).
- [29] R. Ghaffarivardavagh, J. Nikolajczyk, S. Anderson, and X. Zhang, Ultra-open acoustic metamaterial silencer based on Fano-like interference, *Phys. Rev. B* **99**, 024302 (2019).
- [30] X. Wang, X. Luo, B. Yang, and Z. Huang, Ultrathin and durable open metamaterials for simultaneous ventilation and sound reduction, *Appl. Phys. Lett.* **115**, 171902 (2019).
- [31] L. J. Li, B. Zheng, L. M. Zhong, J. Yang, B. Liang, and J. C. Cheng, Broadband compact acoustic absorber with high-efficiency ventilation performance, *Appl. Phys. Lett.* **113**, 103501 (2018).
- [32] J. W. Jung, J. E. Kim, and J. W. Lee, Acoustic metamaterial panel for both fluid passage and broadband soundproofing in the audible frequency range, *Appl. Phys. Lett.* **112**, 041903 (2018).
- [33] M. Yang, G. Ma, Z. Yang, and P. Sheng, Coupled Membranes with Doubly Negative Mass Density and Bulk Modulus, *Phys. Rev. Lett.* **110**, 134301 (2013).
- [34] M. Yang, G. Ma, Y. Wu, Z. Yang, and P. Sheng, Homogenization scheme for acoustic metamaterials, *Phys. Rev. B* **89**, 064309 (2014).
- [35] M. Yang, type Ph.D. thesis, School Hong Kong University of Science and Technology, 2014.
- [36] X. Zhu, K. Li, P. Zhang, J. Zhu, J. Zhang, C. Tian, and S. Liu, Implementation of dispersion-free slow acoustic wave propagation and phase engineering with helical-structured metamaterials, *Nat. Commun.* **7**, 11731 (2016).
- [37] Y. Ding, E. C. Statharas, K. Yao, and M. Hong, A broadband acoustic metamaterial with impedance matching layer of gradient index, *Appl. Phys. Lett.* **110**, 241903 (2017).
- [38] K. Li, B. Liang, J. Yang, J. Yang, and J. C. Cheng, Acoustic broadband metacouplers, *Appl. Phys. Lett.* **110**, 203504 (2017).
- [39] R. Ghaffarivardavagh, J. Nikolajczyk, R. Glynn Holt, S. Anderson, and X. Zhang, Horn-like space-coiling metamaterials toward simultaneous phase and amplitude modulation, *Nat. Commun.* **9**, 1349 (2018).
- [40] S. J. Liang, T. Liu, F. Chen, and J. Zhu, Theoretical and experimental study of gradient-helicoid metamaterial, *J. Sound Vib.* **442**, 482 (2019).